Revealing the impact of polystyrene-functionalization of Au octahedral nanocrystals of different sizes on formation and structure of mesocrystals

Dmitry Lapkin[+], Shweta Singh, Felizitas Kirner, Sebastian Sturm, Dameli Assalauova, Alexandr Ignatenko, Thomas Wiek, Thomas Gemming, Axel Lubk, Knut Müller-Caspary, Azat Khadiev, Dmitri Novikov, Elena V. Sturm, Ivan A. Vartanyants**

Dmitry Lapkin, Shweta Singh, Dameli Assalauova, Alexandr Ignatenko, Azat Khadiev, Dmitri Novikov, Ivan A. Vartanyants
Deutsches Elektronen-Synchrotron DESY, Notkestr. 85, 22607 Hamburg, Germany
E-mail: ivan.vartaniants@desy.de

Felizitas Kirner, Elena V. Sturm
Department of Earth and Environmental Sciences, Section of Crystallography, Ludwig Maximilian University of Munich (LMU), Theresienstr. 41C, 80333 Munich, Germany
E-mail: sturm.elena@lmu.de

Sebastian Sturm, Knut Müller-Caspary
Department of Chemistry and Centre for NanoScience, Ludwig-Maximilians-Universität München (LMU), Butenandtstr. 11, 81377 Munich, Germany

Thomas Wiek, Thomas Gemming, Axel Lubk
Leibniz Institute for Solid State and Materials Research, Helmholtzstraße 20, 01069 Dresden, Germany

[+]*Dmitry Lapkin*
Current address: Institute of Applied Physics, University of Tübingen, Auf der Morgenstelle 10, 72076 Tübingen, Germany

June 26, 2023

Keywords: Gold octahedral nanoparticles; mesocrystals; angular X-ray cross-correlation analysis

Abstract

The self-assembly of anisotropic nanocrystals (stabilized by organic capping molecules) with pre-selected composition, size, and shape allows for the creation of nanostructured materials with unique structures and features. For such a material, the shape and packing of the individual nanoparticles play an important role. This work presents a synthesis procedure for ω-thiol-terminated polystyrene (PS-SH) functionalized gold nanooctahedra of variable size (edge length 37, 46, 58, and 72 nm). The impact of polymer chain length (Mw: 11k, 22k, 43k, and 66k $g \cdot mol^{-1}$) on the growth of colloidal crystals (*e.g.* mesocrystals) and their resulting crystal structure is investigated. Small-angle X-ray scattering (SAXS) and scanning transmission electron microscopy (STEM) methods provide a detailed structural examination of the self-assembled faceted mesocrystals based on octahedral gold nanoparticles of different size and surface functionalization. Three-dimensional angular X-ray cross-correlation analysis (AXCCA) enables high-precision determination of the superlattice structure and relative orientation of nanoparticles in mesocrystals. This approach allows us to perform non-destructive characterization of mesocrystalline materials and reveals their structure with resolution down to the nanometer scale.

1. Introduction

In nanotechnology and materials science, the bottom-up production of nanoparticles with regulated structure and elaborate functionality is constantly a conceptual challenge.[1, 2] The self-assembly of anisotropic nanocrystals (stabilized by organic capping molecules) with pre-selected composition, size, and shape allows for the creation of nanostructured materials with unique structures and features. Colloidal crystals, especially with the defined crystallographic orientation of the nanoparticles (*e.g.* mesocrystals), can demonstrate newly emerging and novel collective properties that cannot occur in any other structure of the same size range.[3] For such a material, the shape and packing of the individual nanoparticles plays an important role.[4-6] The arrangement and orientation of nanoparticles in superlattices depend decisively on their shape.[7-10] Theory predicts the assembly of hard octahedral particles (as non-space filling polyhedra) in a wide variety of fascinating crystalline and liquid-crystalline phases with different orientational and translational orders.[11-13] Furthermore, the rounded corners and curved facets of octahedron-like superballs could play an important role in stabilization of specific assembled phases.[14] In the case of regular hard octahedra, simulation finds the densest packing with a density of 18/19 to be the *Minkowski* lattice.[8, 11-13] With increasing truncation, the packing fraction gradually decreases and the packing switches to a *bcc* or *bct* structure.[11, 15] In experimental work, monoclinic and simple hexagonal superlattices are additionally found as possible packing under different assembly conditions.[8] This emphasizes the high adaptability of the superlattice symmetry on the specific crystallization conditions and functionalization (e.g., type of organic capping molecules) of octahedral particles. The functionalization plays an essential role in the self-assembly of nanoparticles from dispersion due to the interaction of organic ligands between each other and solvent molecules.[16] Nevertheless, most simulation studies do not account for the ligand shell around the inorganic core and are usually performed only with respect to the hard nanoparticle core,

focusing on the study of specific features or specific implementations of mesocrystals.[17-20] Some computational simulations consider the influence of an elastic organic matrix/ligand (i.e., DNA molecules) on the packing arrangement of the building superstructures, yet, only with limited success.[21] Experimentally, it was shown that the self-assembly of Ag nanocubes in 1D and 2D arrays can be tuned by adjusting the surfactant shell.[22, 23] The ligand conformation may be subjected to changes during the assembly process as environmental conditions may change and thus can significantly differ from both dispersed and assembled states, making prognoses about an assembly process and the outcome structure quite complex.

In this work, we studied gold nanoparticles with octahedral shape stabilized by polymer macromolecules with a specific chain length, which not only defines the interparticle distance in assembly, but also affects the effective shape of the nanoparticles, particle-particle, and particle-solvent interactions. This provides an excellent playground system to create ordered plasmonic self-assemblies with potentially tunable structures and properties. We herein present a synthesis procedure for ω-thiol-terminated polystyrene (PS-SH) functionalized gold nanooctahedra of variable size (edge length 37, 46, 58, and 72 nm) and investigate the impact of the polymer chain length (Mw: 11k, 22k, 43k, and 66k $g \cdot mol^{-1}$) on the growth of colloidal crystals (*e.g.* mesocrystals) and their resulting crystal structure. Small-angle X-ray scattering (SAXS) and advanced X-ray and electron imaging methods provide a complete structural examination of the self-assembled superstructures based on nanoparticles of various compositions and forms.[20, 24-29] Angular X-ray cross-correlation analysis (AXCCA), which was recently developed, enables high-precision determination of colloidal crystal structure and relative orientation of nanoparticles in mesocrystals.[30-34] Therefore, in this publication, we combine these two approaches and measure a large part of three-dimensional (3D) reciprocal space in SAXS geometry, including Bragg peaks from the superlattice structure, for individual grains. The AXCCA of the measured 3D scattered intensity

distributions allows revealing the structure of the mesocrystalline grains with a resolution down to the nanometer scale.

2. Results and discussion

2.1. Synthesis of PS-SH functionalized gold octahedral nanoparticles and growth of colloidal crystals

Octahedral nanocrystals (37 – 72 nm edge length) are synthesized in aqueous dispersion according to the literature[35]. These nanoparticles are successfully functionalized by ω-thiol-terminated polystyrene (PS-SH) of different molecular weights (11k g·mol^{-1} - 66k g·mol^{-1}) within the process of a phase transfer to toluene (detailed synthesis parameters can be found in the Supporting Information).[36] UV/Vis spectra before and after functionalization (**Figure S3**, Supporting Information) are recorded to ensure the retention of shape and dispersed state after the phase transfer, no peak broadening is found indicating such processes. Transmission electron microscopy (TEM) investigation of these polystyrene-functionalized particles (**Figure 1a**) further confirms the shape retention and point to an influence of the polymer weight on the packing of the dried nanoparticles. TEM images also indicate that for such small di- or trimers, longer polymer chains (e.g., higher molecular weight) lead to larger distances between the nanocrystal cores and a more random orientation of the nanocrystals towards each other. However, the size of the nanoparticle core also seems to influence the orientation. The shape of the individual gold nanocrystals was verified by high-angle annular dark-field imaging (HAADF) in a scanning transmission electron microscopy (STEM) tomography (**Figure 1 e, Figure S2,** Supporting Information). The degree of truncation along the ⟨100⟩ directions has been estimated to be approximately α = 0.14±0.02, by comparing the deviation of tip-to-tip distances to the ideal octahedron ($\alpha = 1 - d_{t-t}^{real} / d_{t-t}^{ideal}$, where d_{t-t}^{real} and d_{t-t}^{ideal} are the tip-to-tip distance along the ⟨100⟩ directions in a real and ideal octahedra, respectively). The degree of truncation along the ⟨110⟩ directions

is below the resolution limit of tomographic reconstruction. These values are also affected by the tomographic reconstruction resolution, namely because of artefacts (*e.g.* due to a "missing wedge") but should give a good estimate of the level of the edge truncation.

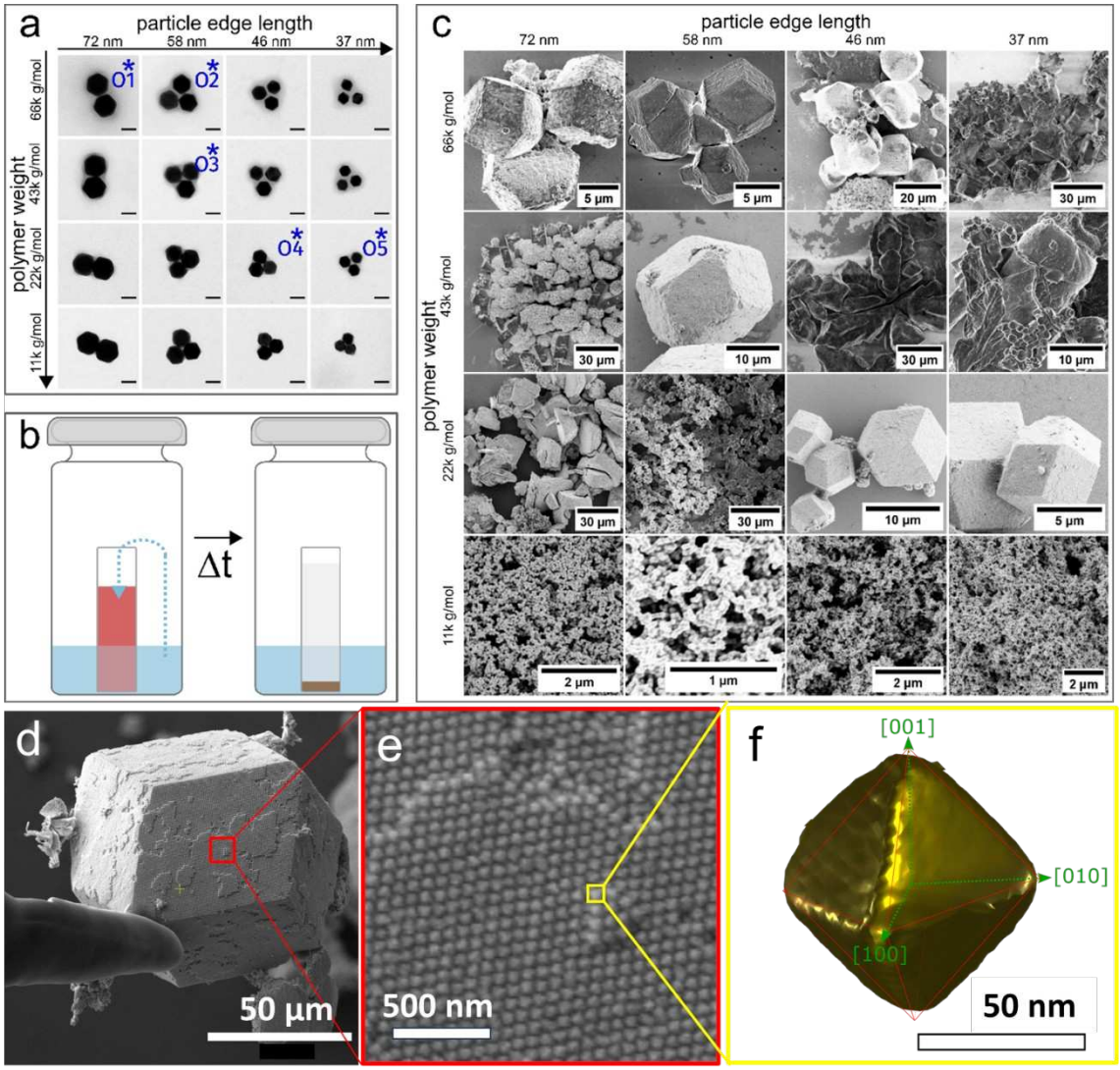

Figure 1. The synthesis of mesocrystals includes the synthesis and functionalization of nanoparticles followed by their assembly. a) Several combinations of core nanooctahedra sizes and ligand polystyrene (PS-SH) chain weights are synthesized. TEM images prove that the octahedral shape of the Au cores is retained during the functionalization process and an influence of the polymer weight on the assembly structure can be observed. The mesocrystalline samples assembled from the nanoparticles with the nanooctahedra sizes and polymer molar weights marked by a blue asterisk are investigated by X-ray diffraction. The scale bar is 50 nm. b) Nanoparticle self-assembly using a gas phase diffusion approach. The sketched setup depicts a closed vial containing the antisolvent and a smaller one containing

the nanoparticle dispersion. Over time, the antisolvent leads to the destabilization of NPs, self-assembly, and discoloration of the dispersion. c) Self-assembled superstructures as collected from the bottom of the vial, investigated by SEM. Superstructure size and morphology vary depending on the polymer/core size combination. Facetted colloidal crystals are found for polymer weights of 22k g·mol^{-1} and above. d) Exemplary SEM image of a mesocrystal of rhombic dodecahedral shape assembled from PS-SH capped octahedral nanoparticles (72 nm edge length, 66k g·mol-1 PS-SH). e) The zoomed image shows the surface structure of the mesocrystal and packing of its nanoparticles. f) HAADF-STEM tomographic reconstruction of an exemplary single octahedral gold nanoparticle (for more details see Figure S2, Supporting Information).

Dynamic light scattering (DLS) measurements are conducted to gain deeper insight into the influence of the polystyrene ligand on the apparent size of the particles in the organic solution (**Figure S4**, Supporting Information). It is found that a longer polymer results in a higher hydrodynamic radius of the nanoparticle meaning that the polymer chains extend further into the dispersing agent, sterically stabilizing the nanoparticles. The comparatively narrow polydispersity index (PDI) from these measurements confirms the conclusion from UV/Vis spectra that the particles are fully dispersed in solution and no aggregation is occurring. All combinations of particle sizes and polymer weights are fully stabilized.

The self-assembly of the particles is induced using a gas-phase diffusion technique with an ethanol mixture as antisolvent (**Figure 1b**).[24] The antisolvent diffuses over the gas phase into the nanoparticle-toluene dispersion and gradually decreases the solvent quality for the stabilizing polystyrene, leading to destabilization, and self-assembly of the particles. The self-assembly is fastest for short polymers and large nanocrystals and slowest for long polymers with small nanocrystals, suggesting a direct influence of the polymer length on the stability of the nanoparticles. Depending on the nanoparticle core size and polymer weight, 3D colloidal crystals or aggregate networks are obtained (**Figure 1c**). For low polymer weight (11k g·mol^{-1}), the destabilization seems to be too fast, preventing an ordered assembly of

nanoparticles and merely leading to aggregation. For polymer weights of 22k g·mol^{-1} and above, 3D superstructures are built. In general, we observe the following tendency: longer polymers and smaller nanoparticles produce larger superstructures. This emphasizes the crucial influence of the nanoparticle stability on the self-assembly process and the necessity of the nanoparticles to be able to attach and detach to a building superstructure to build nicely defined superstructures. Three-dimensional superstructures with well-defined faceting (rhombic dodecahedral shape) and suitable size are obtained for 5 polymer-nanocrystal combinations (**Figure 1d, Figure S5**, Supporting Information): a) O1 sample (72 nm edge length, 66k g·mol^{-1} PS-SH). b) O2 sample (58 nm edge length, 66k g·mol^{-1} PS-SH). c) O3 sample (58 nm edge length, 43k g·mol^{-1} PS-SH). d) O4 sample (46 nm edge length, 22k g·mol^{-1} PS-SH). e) O5 sample (37 nm edge length, 22k g·mol^{-1} PS-SH). These samples are chosen for further X-ray structure analysis, as it was possible to pick samples with a diameter of approximately 5 – 10 µm as necessary for the X-ray diffraction (XRD) experiment. Thereby, modification or destruction of the sample by e.g. FIB preparation procedures are circumvented. The selected facetted colloidal crystals were mounted onto tungsten needles and glued with SEMGLU glue (Kleindiek Nanotechnik GmbH) using a Zeiss 1540XB CrossBeam focused-ion-beam scanning-electron-microscope (FIB SEM) (see **Figure 1d**, and **Figure S5,** Supporting Information).

2.2. Structural characterization of faceted mesocrystals

The XRD experiment (see **Figure 2** for the schematic layout of the X-ray experimental setup and Methods section for further details) was performed on the five selected faceted mesocrystals (**Figure 1** and **Figure S5,** Supporting Information). The 3D reciprocal space maps of two samples composed of the biggest (O1) and smallest (O5) Au nanooctahedra are presented in **Figure 3a–b** (reciprocal space maps for all samples are given in **Figure S6**, Supporting Information). These 3D maps were obtained from the individual two-dimensional (2D) diffraction patterns of the analyzed samples measured at different angles by interpolating

them onto a 3D orthogonal grid with a voxel size of 0.0015 nm^{-1}. The average radial profiles of the measured scattered intensity distributions and average radial profiles of the intensity between the Bragg peaks for all measured samples are shown in **Figure 3c**. As one can observe from these profiles, with the decreasing size of the nanooctahedra in the samples O1 – O5, the Bragg peaks shift towards the higher *q*-values indicating the shrinkage of the superlattice unit cell of the mesocrystals. This is valid in all cases except for the samples O2 and O3 composed of nanooctahedra of the same size. A similar trend is observed for intensities taken between the Bragg peaks. These curves mostly resemble the form-factor of individual Au octahedra, though affected by the structure factor at low *q*-values. As it is well seen from **Figure 3c**, the form factor oscillations have a smaller period for the samples composed of bigger nanooctahedra.

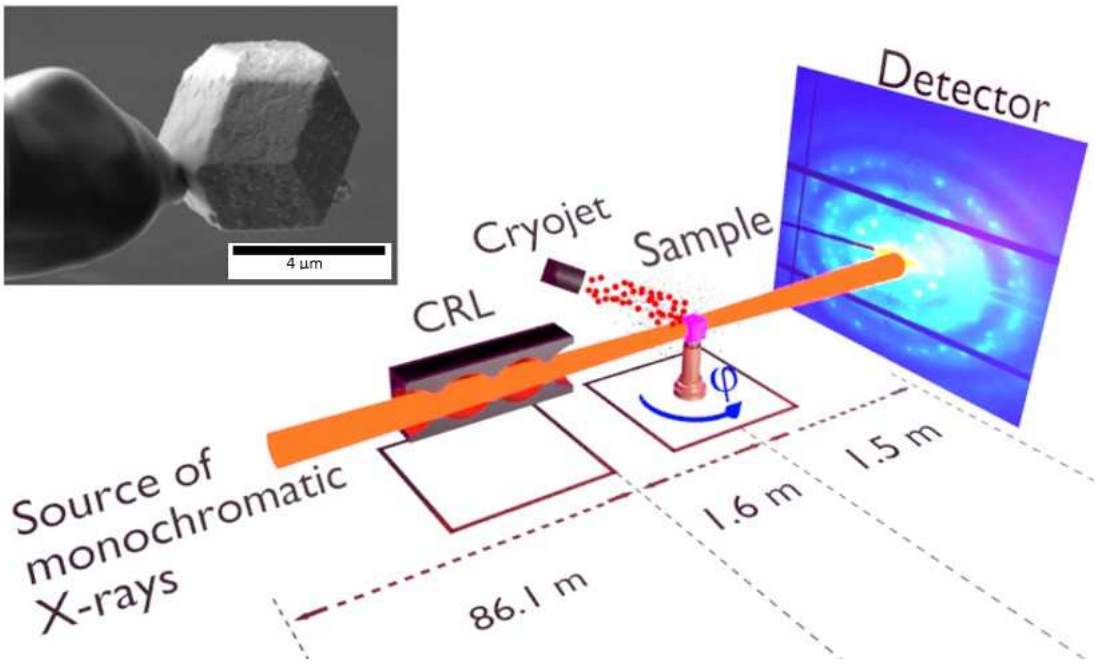

Figure 2. The X-ray diffraction experimental setup. Compound Refractive Lenses (CRLs) are used to focus a monochromatic X-ray beam at the sample position. A liquid nitrogen cryojet was used to cool the sample and prevent the radiation damage. An X-Spectrum Lambda 750K detector was positioned downstream at a distance of 1.5 m from the sample to measure the far-field diffraction patterns. The sample was rotated around the vertical axis, and scattering patterns were measured at different angles in the range of $\varphi=0-180°$ with the step of $\Delta\varphi=0.5°$. In the inset, an exemplary SEM image of a single mesocrystalline grain fixed on a tungsten tip as measured in the experiment is shown.

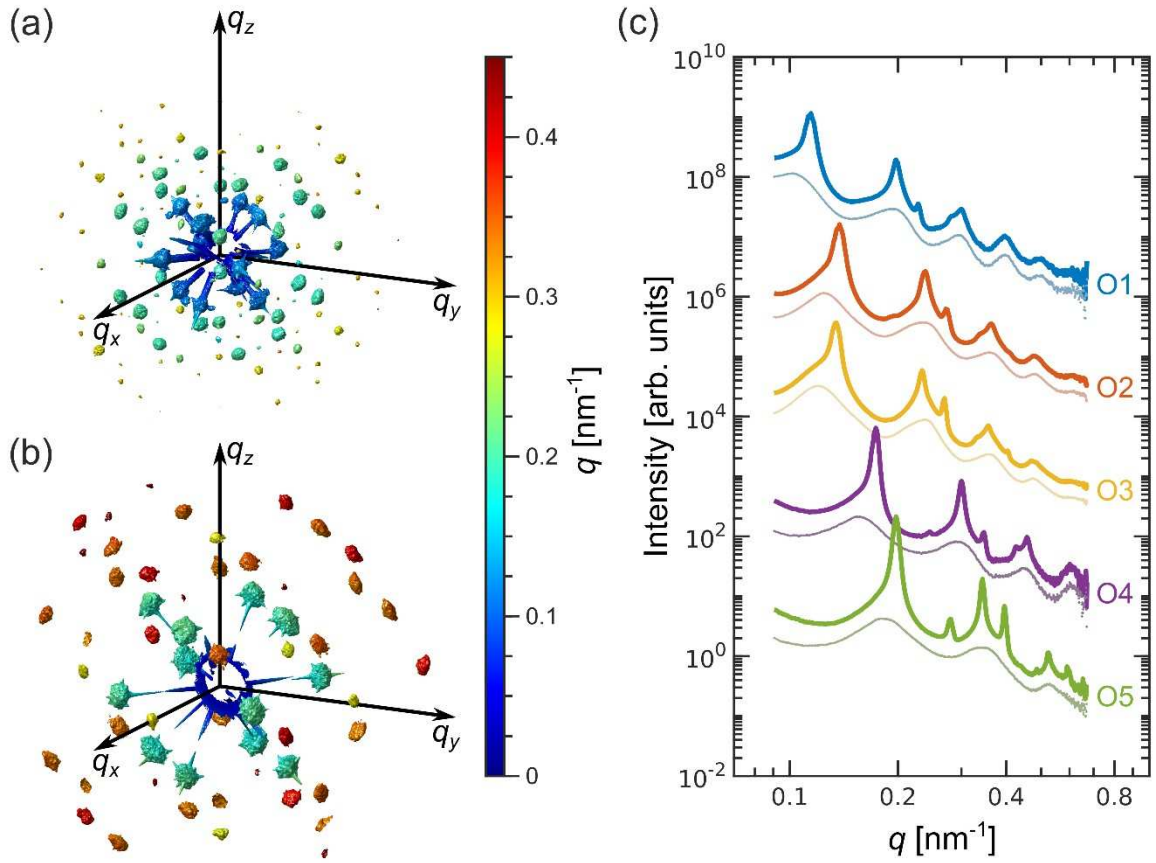

Figure 3. (a, b) Examples of the measured scattered intensity distributions in 3D reciprocal space for O1 (a) and O5 (b) mesocrystalline samples. The isosurfaces are rendered for the same arbitrary isovalue. The colors indicate the distance from the origin of the reciprocal space (q-values). (c) Average radial profiles of the measured scattered intensity distributions (thick lines) and average radial profiles between the Bragg peaks (thin lines) for all measured samples shown in log-log scale. The resolution is 0.005 nm^{-1}. The profiles are shifted vertically for clarity.

To extract the unit cell parameters, we applied AXCCA to the 3D intensity distribution measured for all samples (see Methods section for a description of the AXCCA). Examples of the obtained cross-correlation functions (CCFs) for the samples O1 and O5 are shown in **Figure 4** (the results of AXCCA for all samples are shown in **Figure S7,** Supporting Information). The CCFs $C(q_1,q_2,\Delta)$ were calculated as follows. The value of the first momentum transfer q_1 was fixed to the position of the first Bragg peak (see Table 1 for the values) and the value of the second momentum transfer q_2 was varied in the range of $q_2 = 0.07 - 0.50$ nm^{-1} with a step size of 0.005 nm^{-1}. The CCFs represented in **Figure 4** are shown as functions of q_2 and Δ. In this figure, bright yellow spots represent the correlation peaks occurring between the first order Bragg peaks and all others. The CCFs also contain stripe-like features at low q-values corresponding to the correlations with the crystal

truncation rods produced by {110} facets of rhombic dodecahedral mesocrystalline grains. We note that we did not fully cover reciprocal space for $q > 0.42$ nm^{-1} due to the experimental geometry which explains the absence of some correlation peaks in the CCFs calculated for these q-values.

We assumed that the real space structure for all measured samples is body-centered cubic (*bcc*). We performed modeling of the correlation peak positions corresponding to this structure and optimized the unit cell parameter to fit the experimental peak positions (see for details Ref.[37] and section S3.4, Supporting Information). The correlation peak positions for the optimized structures are indicated in **Figure 4** by red circles. The corresponding unit cell parameters for all samples are summarized in **Table 1**.

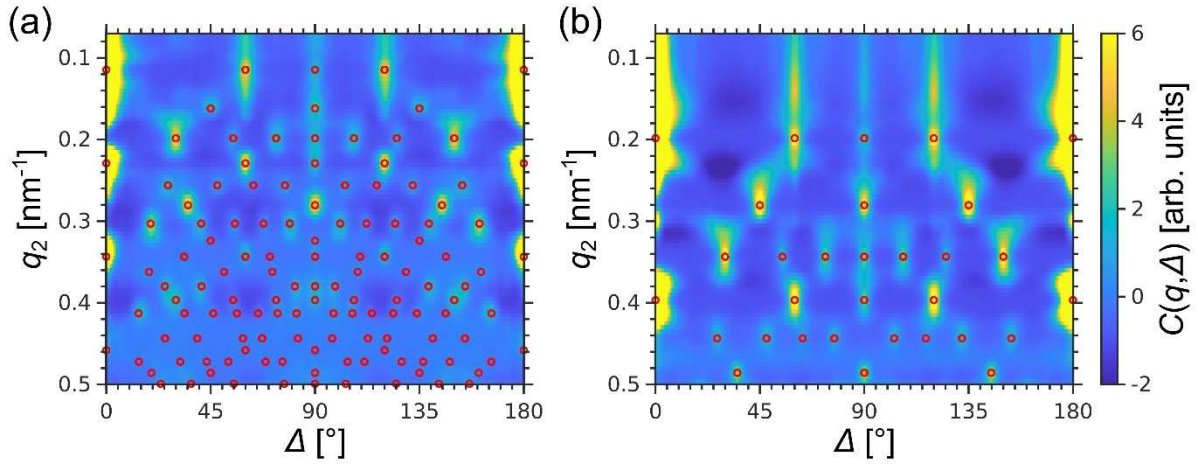

Figure 4. 2D maps of cross-correlation functions $C(q_1, q_2, \Delta)$ calculated for the samples O1 (a) and O5 (b). Red circles represent the peak positions for the optimized bcc structure. The cross-correlation functions are calculated for the q_1 value corresponding to the first Bragg peak position (see Table 1 for the values) and q_2 varying in the range of 0.07 – 0.50 nm^{-1} with the step size of 0.005 nm^{-1}.

The deviation of the unit cell parameters within each sample were estimated from the Bragg peak widths using the Williamson-Hall method (the details of the analysis are given in section S3.5, Supporting Information).[38] The extracted radial superlattice distortion g_q provides the dispersion of the unit cell parameter in a single sample as $\delta a = g_q \cdot \langle a \rangle$, where $\langle a \rangle$ is the average unit cell parameter extracted by the AXCCA. The extracted angular lattice distortion g_φ resembles the dispersion in the angular unit cell parameter as $\delta\varphi = g_\varphi \cdot 180°/\pi$. Thus, the extracted dispersion in radial and angular unit cell parameters for all samples is provided in **Table 1** as an error.

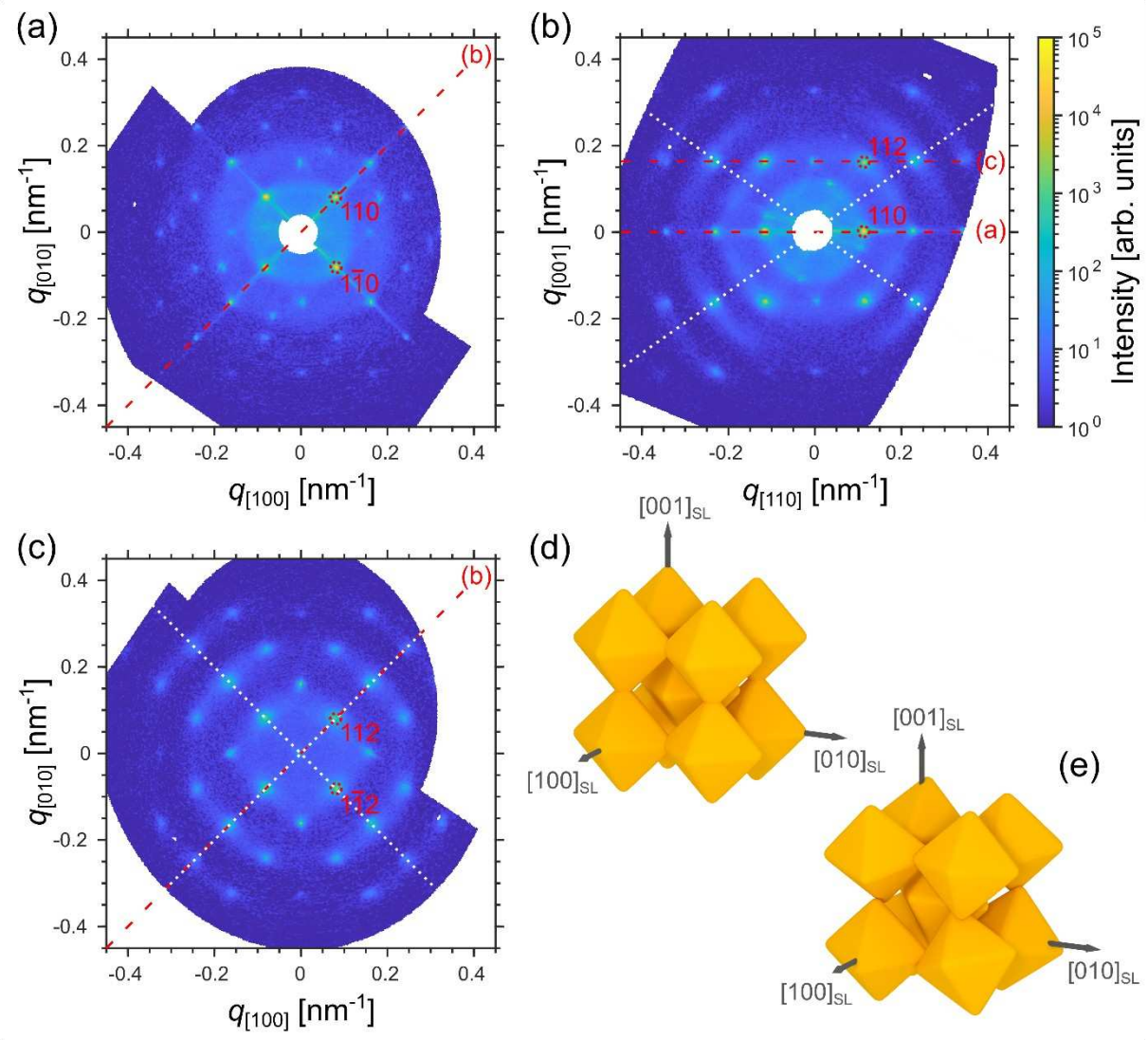

Figure 5. a-c) Cuts through the measured 3D intensity distributions for the O1 sample: (a) through the reciprocal space origin and normal to the $[001]_{SL}$ axis, (b) through the reciprocal space origin and normal to the $[1\bar{1}0]_{SL}$ axis, and (c) through the 002 Bragg peak and normal to the $[001]_{SL}$ axis (the offset along the $[001]_{SL}$ axis is 0.162 nm^{-1}). The red dashed lines indicate the cuts shown in the other panels. Along with the Bragg peaks, anisotropic features of the form factor of the gold octahedral nanoparticles are well visible. The white dotted lines in panel (b) indicate the $[111]_{SL}$ and $[11\bar{1}]_{SL}$ axes, and in panel (c) – the $[110]_{SL}$ and $[1\bar{1}0]_{SL}$ axes. (d, e) The real space models of a *bcc* superlattice unit cell with the ideal angular orientation of the nanooctahedra (d) and with a certain degree of angular disorder (e). The orientation of the octahedral nanoparticles within the superlattice is revealed by analysis of the anisotropic form factor.

After analysis of the Bragg peaks originating from the superlattice, we turn our attention to the angular orientation of individual octahedra inside the superlattice. The octahedral shape of the nanoparticles is defined by eight $\{111\}_{AL}$ facets that lead to a highly anisotropic form factor of a single nanooctahedron with fringes normal to the facets. The cuts of the 3D intensity distribution through the crystallographic planes of the superlattice, presented for O1 sample in **Figure 5a–c** (the cuts for other samples are given in **Figures S12.1 – S12.4**, Supporting Information), show the presence of the anisotropic form factor features. This finding confirms that the nanooctahedra inside the superlattice are mutually oriented. As can be seen from **Figure 5b**, the fringes normal to the nanooctahedra facets are oriented along the $\langle 111 \rangle_{SL}$ axes. Alignment of the form factor features with the $\langle 110 \rangle_{SL}$ axes in **Figure 5c** confirms that all $\{111\}_{AL}$ nanooctahedron facets are oriented with the $\langle 111 \rangle_{SL}$ superlattice axes. Thus, all $[hkl]_{AL}$ atomic lattice axes are aligned along the corresponding $[hkl]_{SL}$ superlattice axes as shown in **Figure 5d**. Comparison of the experimentally measured scattering patterns with the simulated ones for the given orientation of nanooctahedra (see section S3.6, Supporting Information) confirms our observations. Broadening of the form factor features in the azimuthal direction implies orientational disorder of the nanooctahedra around their ideal orientation as shown in **Figure 5e**. By visual inspection of the measured scattered intensity distribution with the simulated ones for different degree of orientational disorder, we concluded that the nanooctahedra have a normal distribution around the ideal orientation with a standard deviation of $\delta\varphi \approx 15°$.

Although the *bcc* superlattice structure with tip-to-tip oriented nanooctahedra does not provide the highest possible packing density for nanooctahedra, it was previously reported for mesocrystals consisting of nanooctahedra capped by organic ligands.[15] Such a structure is believed to ensure the packing of ligands in the voids formed by the facets of adjacent nanooctahedra. This speculation is supported by the difference in the ligand density on the facets and close to tips.[6] The lower ligand density at the tips facilitate the tip-to-tip orientation of the nanooctahedra in the *bcc* superlattice.

The revealed angular orientation of the nanooctahedra makes it possible to compare the defined superlattice unit cell parameters with the nanooctahedra dimensions. First, we extracted the nanooctahedra dimensions from the TEM measurements. An average edge length l was determined from the projections of individual nanooctahedra along the $[111]_{AL}$ direction for each sample (see section S1.2, Supporting Information). From the edge length, the facet-to-facet distance d_{f-f}, and the ideal tip-to-tip distance d_{t-t}^{ideal} were calculated as

$d_{f-f}=\sqrt{6}l/3$ and $d_{t-t}^{ideal}=\sqrt{2}l$, respectively. All obtained values are summarized in **Table 1**. We note that the obtained values correspond to dimensions of an ideal nanooctahedron and do not take into account truncation of the nanooctahedra corners, which is visible on the TEM images (see **Figure S1**, Supporting Information)) and confirmed by the HAADF-TEM tomography reconstruction (see **Figure 1f**). The facet-to-facet distance d_{f-f} is not affected by the truncation and thus corresponds to the actual size of the nanooctahedra.

As it follows from **Figure 5d**, the nearest neighbor nanooctahedra along the $\langle 111\rangle_{SL}$ directions face each other with their facets. The nearest-neighbor distance d_{NN} in the *bcc* superlattice can be calculated from the unit cell parameter a as $d_{NN}=\sqrt{3}a/2$. The obtained values d_{NN} given in **Table 1** can be compared to the facet-to-facet distance d_{f-f} obtained from the TEM measurements as described above. The difference of these values corresponds to the spacing between the nanooctahedra and is mainly due to the interspacing polymer. As expected, the facet-to-facet distance is smaller than the nearest neighbor distance for all studied samples with the interparticle distance of about 8 nm regardless of the nanooctahedra size.

In its turn, the adjacent nanooctahedra along the $\langle 100\rangle_{SL}$ axes touch each other with their tips. The unit cell parameters a, equal to the distance between the adjacent nanooctahedra in these directions and summarized in **Table 1,** can be directly compared to the tip-to-tip distance d_{t-t}^{ideal} obtained from the TEM measurements. Apparently, the tip-to-tip distances are larger than the unit cell parameters for all the samples; the difference gradually decreases from about 24 nm for the biggest nanooctahedra down to about 7 nm for the smallest ones. For an ideal lattice of untruncated nanooctahedra, this would lead to a topologically unfavorable structure. In the experiment, we deal with nanooctahedra with slightly truncated tips that lead to the reduction of the particle "overlap". Moreover, the observed angular disorder enables more effective packing where the nanooctahedra touch the next ones not directly with their tips but with their edges or facets close to the tips as shown in **Figure 5e**. Thus, the truncation and angular disorder of the nanooctahedra enable the otherwise topologically unfavourable structure.

Table 1. The parameters of the samples O1 – O5 as determined from the TEM, AXCCA, and Williamson-Hall method. The edge length l was measured from the TEM, error bars are the standard deviation of a few measured samples. The tip-to-tip distance d_{t-t}^{ideal} and facet-to-facet distance d_{f-f} were calculated from the edge length as described in section S1.3 of Supporting

Information. The first Bragg peak q-value is obtained from the average radial profiles shown in Figure 3c. The unit cell parameter a is determined from the AXCCA method and error bars are deduced as the standard deviation obtained from the Williamson-Hall method. The nearest-neighbor distance d_{NN} is obtained from the unit cell parameter a as $d_{NN}=\sqrt{3}a/2$. The angular unit cell distortion and error bars are obtained from the Williamson-Hall method.

SAMPLE	O1	O2	O3	O4	O5
Nanooctahedra edge length *l* from TEM images [nm]	72.0 ± 1.6	58.4 ± 1.8	58.4 ± 1.8	46.3 ± 1.4	36.7 ± 1.1
Tip-to-tip distance d_{t-t}^{ideal} calculated for ideal nanooctahedron [nm]	98.5 ± 2.45	79.5 ± 2.5	79.5 ± 2.5	63.8 ± 2.3	51.5 ± 1.9
Facet-to-facet distance $d_{f\text{-}f}$ [nm]	58.8 ± 1.3	47.7 ± 1.5	47.7 ± 1.5	37.8 ± 1.1	30.0 ± 0.9
First Bragg peak q-value [nm^{-1}]	0.114	0.137	0.134	0.173	0.197
Optimized unit cell parameter a [nm]	77.6 ± 0.9	64.5 ± 1.4	66.0 ± 1.0	51.2 ± 0.5	44.8 ± 0.6
Nearest-neighbor distance d_{NN} [nm]	67.2 ± 0.8	55.9 ± 1.2	57.2 ± 0.9	44.3 ± 0.4	38.8 ± 0.5
Angular distortion of the unit cell [°]	1.0 ± 0.3	0.9 ± 0.3	0.9 ± 0.4	1.3 ± 0.6	0.9 ± 0.6

3. Conclusions

In summary, we presented a synthesis procedure for PS-SH functionalized gold octahedral nanoparticles of variable size (edge length 37, 46, 58, and 72 nm) and investigated the impact of polymer chain length (Mw: 11k, 22k, 43k, and 66k $g{\cdot}mol^{-1}$) on the growth of faceted colloidal crystals (i.e., mesocrystals) from toluene solution using a gas-phase diffusion technique. To resolve the structure of the grown rhombicdodecahedral mesocrystals we performed an XRD experiment in SAXS geometry at a synchrotron source. By applying the AXCCA method, we identified that in all cases nanocrystals self-assemble in a *bcc*

superstructure, where gold octahedral nanoparticles are predominantly oriented tip-to-tip. This, at first, seemingly unfavorable orientational order is possible due to a slight truncation of nanooctahedra along the ⟨100⟩ direction and their angular disorder within the superlattice, which enables a more effective packing. HAADF-STEM tomographic reconstruction revealed the degree of octahedra truncation along ⟨100⟩ directions to be approximately $\alpha = 0.14 \pm 0.02$.

This experimental system provides an important contribution in understanding the packing behavior of octahedral nanoparticles with tunable surface properties (due to the functionalization by polymers with variable chain length) and reveals conditions for crystallization of the faceted mesocrystals. The latter is important for studying of optical properties of such highly ordered assemblies with a tunable distance between the plasmonic nanoparticles (due to surfactants with different polymer chain length) and different coordination geometries. This coordination is determined not only by the symmetry of the superlattice, but also by the location of nanoparticles within the bulk volume, and the orientation of vertices of the faceted mesocrystals. The exact coordination structure of faceted mesocrystals can be further explored in the future by Coherent X-ray Diffraction Imaging (CXDI), which can achieve nanoscale spatial resolution, allowing the presence of different types of structural defects to be revealed.

4. Experimental Section/Methods

Synthesis and Functionalization of Polystyrene-stabilized Au Nanooctahedra

The synthesis of the nanocrystals is conducted as published previously,[35] adaptions for the adjustment of the particle morphology were made. The functionalization of the gold nanooctahedra is adapted from a procedure described by Sánchez-Iglesias et al.[36] Four different polystyrene weights are used for this functionalization (11k $g \cdot mol^{-1}$, 22k $g \cdot mol^{-1}$, 43k $g \cdot mol^{-1}$, and 66k $g \cdot mol^{-1}$). The nanoparticle dispersion is centrifuged at 9000 rpm for 5 min, the supernatant is removed and the sedimented particles are redispersed in 10 mL water. The particles are then concentrated to 1 mL (concentration of Au is 2 mg/mL). This dispersion is added to a THF solution containing one ω-thiol-terminated polystyrene chain per nm^2 surface of the added nanoparticles (estimated from TEM size investigation and assuming ideal octahedral shape) and mixed thoroughly. The dispersion is left undisturbed for 12 h and

subsequently centrifuged at 9000 rpm for 5 min, the supernatant is discarded and the particles are redispersed in 10 mL THF. After another round of centrifugation, the supernatant is removed and the particles are redispersed in 1 mL of toluene. This second round of centrifugation is crucial to reduce the amount of water present in the system that would otherwise lead to the irreversible aggregation of the particles upon addition of toluene. The functionalized particles were investigated by TEM (**Figure 1**), UV/Vis (**Figure S1**, Supporting Information), and DLS (**Figure S3**, Supporting Information).

Self-assembly by gas-phase diffusion

The nanocubes were assembled to mesocrystals using a gas-phase diffusion technique (**Figure S1** and section S1.4, Supporting Information).[29] 400 µL of 2 mg/mL nanocube dispersion in toluene was filled in a 1 mL flat bottom vial. This small vial was then placed in a larger vial containing an antisolvent consisting of 1 mL ethanol and 1 mL toluene. The larger vial was sealed creating a closed system. The antisolvent diffuses into the nanoparticle dispersion destabilizing the particles and leading to self-assembly indicated by a gradual discoloration of the dispersion. After 3 weeks, the solution was fully discolored. The solution was then overlaid with 200 µL of ethanol to discourage redissolution of the assembled superstructures in the collection process of the self-assemblies. The clear solution was removed using a syringe. The superstructures laying on the bottom were then collected with the residual solvent using a micropipette and placed on a silicon snipped for further investigation. An overview of the self-assembled structures is provided in **Figure 1c**.

X-ray Scattering Experiment

The experiment took place at In-situ X-ray diffraction and imaging beamline P23 of the PETRA III storage ring at DESY (Germany). Monochromatic X-rays with a photon

energy of 8.32 keV ($\lambda = 0.149$ nm) were focused by beryllium (Be) compound refractive lenses (CRLs). At this photon energy, the approximate beam size in the vertical direction was 7 – 12 μm (Full Width at Half-Maximum, FWHM) and about 21 – 36 μm (FWHM) in the horizontal direction. This allowed the X-ray beam to completely cover the colloidal crystal grains which have sizes ranging between 5 – 10 μm (compare with **Figure S5**, Supporting Information). The mesocrystal grains were mounted on a tungsten tip and rotated around the vertical axis in steps of 0.5° in the range of 0 – 180°. For each angular position, 2D far-field scattering patterns were collected by the X-Spectrum Lambda 750K GaAs detector, which was positioned 1.497 m downstream from the sample. Series of two frames of 1 s exposure each were measured at each angular position, resulting in a total of 2 s exposure. The sample was cooled by a liquid nitrogen cryojet (OXFORD Cryostream 700) to minimize radiation damage to the organic ligands (stabilizing nanocrystals), which might lead to nanoparticle coalescence and the loss of superlattice organization. The collected 2D patterns were interpolated onto a 3D orthonormal grid with the voxel size of 0.0015 nm^{-1}.

Angular X-ray Cross-Correlation Analysis

We used the AXCCA method modified for applications to 3D intensity distributions as described in Ref.[37]. The method is based on analysis of two-point CCFs $C(q_1,q_2,\Delta)$ calculated for measured scattered intensity distribution in 3D reciprocal space as

$$C(q_1, q_2, \Delta) = \left\langle \tilde{I}(q_1)\tilde{I}(q_2)\delta\left(\frac{q_1 \cdot q_2}{\|q_1\|\|q_2\|} - \cos\Delta\right)\right\rangle, \quad \textbf{(1)}$$

where $\tilde{I}(q_1)$ and $\tilde{I}(q_2)$ are normalized intensities taken at the momentum transfer positions $\mathbf{q_1}$ and $\mathbf{q_2}$ in 3D reciprocal space and $\delta(x)$ is a Dirac delta-function. The averaging is performed over the all momentum transfer positions of $\mathbf{q_1}$ and $\mathbf{q_2}$ with the lengths $q_1 = \|\mathbf{q_1}\|$ and $q_2 = \|\mathbf{q_2}\|$, respectively. The intensities are normalized to the mean values at the corresponding q-value as

$$\tilde{I}(q_i) = \frac{I(q_i) - \langle I(q_i) \rangle}{\langle I(q_i) \rangle}, i = 1,2 \quad \textbf{(2)}$$

where averaging is performed over all positions corresponding to $\mathbf{q}_i$ with the length $q_i = \|\mathbf{q}_i\|$.

In this work, we calculated CCFs $C(q_1,q_2,\Delta)$ for a fixed momentum transfer value q_1 corresponding to the first Bragg peak position and varying momentum transfer values q_2. These CCFs are represented as corresponding maps in (q_2,Δ)-coordinates.

Supporting Information

Supporting Information is available from the Wiley Online Library or the corresponding authors.

Acknowledgments

We acknowledge DESY (Hamburg, Germany), a member of the Helmholtz Association HGF, for the provision of experimental facilities. Parts of this research were carried out at PETRA III P23 "In situ X-ray diffraction and imaging beamline" and we would like to thank P23 beamline engineer Atula Poduval for assistance during the beamtime. Beamtime was allocated for proposal I-20210458 . The authors want to acknowledge the support of the core facilities nano.lab (Nanostructure Laboratory) and PAC (Particle Analysis Centre) of the University of Konstanz. F. K. and E. V. S acknowledge the DFG (Deutsche Forschungsgemeinschaft) for financial support (SFB 1214. Project B1).

Conflict of interest

The authors declare no conflict of interest.

Data availability

The X-ray data that support the findings of this study are openly available in Zenodo.org at https://zenodo.org/record/8060535

Author contributions

D. L. and S. S. contributed equally to this work. F.K. synthesized the nanoparticles and prepared the samples. S. St., Th. W., Th.G., E.V.S. and A.L. prepared the samples for X-ray measurements. S. St., E.V.S. and K. M-C. performed HAADF-STEM measurements, D. L., S. S., D. A., A. I., A. Kh., D. N., and I.A.V. performed the X-ray scattering experiment. D. L. and S. S. analyzed the collected X-ray data. E.V.S. and I.A.V. conceived and supervised the project. D. L., S. S., F. K., S. St., E. V. S. and I. A. V. wrote the manuscript with input from all authors. All authors have given approval to the final version of the manuscript.

Received: ((will be filled in by the editorial staff))

Revised: ((will be filled in by the editorial staff))

Published online: ((will be filled in by the editorial staff))

References

1. Sturm , E. V.; Cölfen, H., Mesocrystals: Past, Presence, Future. *Crystals* **2017,** *7* (7), 207.

2. Talapin, D. V.; Shevchenko, E. V., Introduction: Nanoparticle Chemistry. *Chemical Reviews* **2016,** *116* (18), 10343-5.

3. Sturm, E. V.; Cölfen, H., Mesocrystals: structural and morphogenetic aspects. *Chemical Society Reviews* **2016,** *45* (21), 5821-5833.

4. Bian, K.; Schunk, H.; Ye, D.; Hwang, A.; Luk, T. S.; Li, R.; Wang, Z.; Fan, H., Formation of self-assembled gold nanoparticle supercrystals with facet-dependent surface plasmonic coupling. *Nature communications* **2018,** *9* (1), 2365.

5. Schultz, J.; Kirner, F.; Potapov, P.; Büchner, B.; Lubk, A.; Sturm, E. V., Tailoring Plasmonics of Au@Ag Nanoparticles by Silica Encapsulation. *Advanced Optical Materials* **2021,** *9* (22), 2101221.

6. Huang, X.; Zhu, J.; Ge, B.; Gerdes, F.; Klinke, C.; Wang, Z., In Situ Constructing the Kinetic Roadmap of Octahedral Nanocrystal Assembly Toward Controlled Superlattice Fabrication. *Journal of the American Chemical Society* **2021,** *143* (11), 4234-4243.

7. Ahmed, N. K.; van Anders, G.; Chen, E.; Glotzer, S. A., Crossover Behavior in the Packing and Assembly of Concave Hard Spheres. **2015**.

8. Gong, J.; Newman, R. S.; Engel, M.; Zhao, M.; Bian, F.; Glotzer, S. C.; Tang, Z., Shape-dependent ordering of gold nanocrystals into large-scale superlattices. *Nat Commun* **2017,** *8*, 14038.

9. Liao, C.-W.; Lin, Y.-S.; Chanda, K.; Song, Y.-F.; Huang, M. H., Formation of Diverse Supercrystals from Self-Assembly of a Variety of Polyhedral Gold Nanocrystals. *Journal of the American Chemical Society* **2013,** *135* (7), 2684-2693.

10. Xu, Z.; Yang, J.; Ding, Y.; Zhao, Y.; Li, J.; Hu, B.; Xia, C., Packing and void structures of octahedral, dodecahedral and icosahedral granular particles. *Granular Matter* **2021,** *23* (4), 88.

11. Gantapara, A. P.; de Graaf, J.; van Roij, R.; Dijkstra, M., Phase Diagram and Structural Diversity of a Family of Truncated Cubes: Degenerate Close-Packed Structures and Vacancy-Rich States. *Physical Review Letters* **2013,** *111* (1), 015501.

12. Minkowski, H., Dichteste gitterförmige Lagerung kongruenter Körper. *Nachr. Ges. Wiss. Göttingen, Math.-Phys. Kl.* **1904,** *1904*, 311-355.

13. Torquato, S.; Jiao, Y., Dense packings of the Platonic and Archimedean solids. *Nature* **2009,** *460* (7257), 876-879.

14. Ni, R.; Gantapara, A. P.; de Graaf, J.; van Roij, R.; Dijkstra, M., Phase diagram of colloidal hard superballs: from cubes via spheres to octahedra. *Soft Matter* **2012,** *8* (34), 8826-8834.

15. Zhang, J.; Luo, Z.; Quan, Z.; Wang, Y.; Kumbhar, A.; Smilgies, D.-M.; Fang, J., Low Packing Density Self-Assembled Superstructure of Octahedral Pt3Ni Nanocrystals. *Nano Letters* **2011,** *11* (7), 2912-2918.

16. Schlotheuber né Brunner, J.; Maier, B.; Thomä, S. L. J.; Kirner, F.; Baburin, I. A.; Lapkin, D.; Rosenberg, R.; Sturm, S.; Assalauova, D.; Carnis, J.; Kim, Y. Y.; Ren, Z.; Westermeier, F.; Theiss, S.; Borrmann, H.; Polarz, S.; Eychmüller, A.; Lubk, A.; Vartanyants, I. A.; Cölfen, H.; Zobel, M.; Sturm, E. V., Morphogenesis of Magnetite Mesocrystals: Interplay between Nanoparticle Morphology and Solvation Shell. *Chemistry of Materials* **2021,** *33* (23), 9119-9130.

17. Dreyer, A.; Feld, A.; Kornowski, A.; Yilmaz, E. D.; Noei, H.; Meyer, A.; Krekeler, T.; Jiao, C.; Stierle, A.; Abetz, V.; Weller, H.; Schneider, G. A., Organically linked iron oxide nanoparticle supercrystals with exceptional isotropic mechanical properties. *Nature Materials* **2016,** *15* (5), 522-8.

18. Boles, M. A.; Engel, M.; Talapin, D. V., Self-Assembly of Colloidal Nanocrystals: From Intricate Structures to Functional Materials. *Chemical Reviews* **2016,** *116* (18), 11220-89.

19. Tebbe, M.; Lentz, S.; Guerrini, L.; Fery, A.; Alvarez-Puebla, R. A.; Pazos-Perez, N., Fabrication and optical enhancing properties of discrete supercrystals. *Nanoscale* **2016,** *8* (25), 12702-9.

20. André, A.; Zherebetskyy, D.; Hanifi, D.; He, B.; Samadi Khoshkhoo, M.; Jankowski, M.; Chassé, T.; Wang, L.-W.; Schreiber, F.; Salleo, A.; Liu, Y.; Scheele, M., Toward Conductive Mesocrystalline Assemblies: PbS Nanocrystals Cross-Linked with Tetrathiafulvalene Dicarboxylate. *Chemistry of Materials* **2015,** *27* (23), 8105-8115.

21. O'Brien, M. N.; Lin, H. X.; Girard, M.; Olvera de la Cruz, M.; Mirkin, C. A., Programming Colloidal Crystal Habit with Anisotropic Nanoparticle Building Blocks and DNA Bonds. *Journal of the American Chemical Society* **2016,** *138* (44), 14562-14565.

22. Rabin, O., Judging a nanocube by its cover. *Nature Nanotechnology* **2012,** *7* (7), 419-420.

23. Gao, B.; Arya, G.; Tao, A. R., Self-orienting nanocubes for the assembly of plasmonic nanojunctions. *Nature Nanotechnology* **2012,** *7* (7), 433-7.

24. Simon, P.; Rosseeva, E.; Baburin, I. A.; Liebscher, L.; Hickey, S. G.; Cardoso-Gil, R.; Eychmuller, A.; Kniep, R.; Carrillo-Cabrera, W., PbS-organic mesocrystals: the relationship between nanocrystal orientation and superlattice array. *Angew Chem Int Ed Engl* **2012,** *51* (43), 10776-81.

25. Zhang, J.; Zhu, J.; Li, R.; Fang, J.; Wang, Z., Entropy-Driven Pt3Co Nanocube Assembles and Thermally Mediated Electrical Conductivity with Anisotropic Variation of the Rhombohedral Superlattice. *Nano Letters* **2017,** *17* (1), 362-367.

26. Bian, K.; Li, R.; Fan, H., Controlled Self-Assembly and Tuning of Large PbS Nanoparticle Supercrystals. *Chemistry of Materials* **2018,** *30* (19), 6788-6793.

27. Huang, X.; Wang, Z., Supercrystallography-Based Decoding of Structure and Driving Force of Nanocrystal Assembly. *Materials* **2019,** *12* (22), 3771.

28. Lv, Z. P.; Kapuscinski, M.; Bergstrom, L., Tunable assembly of truncated nanocubes by evaporation-driven poor-solvent enrichment. *Nature Communications* **2019,** *10* (1), 4228.

29. Zhu, H.; Fan, Z.; Yu, L.; Wilson, M. A.; Nagaoka, Y.; Eggert, D.; Cao, C.; Liu, Y.; Wei, Z.; Wang, X.; He, J.; Zhao, J.; Li, R.; Wang, Z.; Grunwald, M.; Chen, O., Controlling Nanoparticle Orientations in the Self-Assembly of Patchy Quantum Dot-Gold Heterostructural Nanocrystals. *J Am Chem Soc* **2019,** *141* (14), 6013-6021.

30. Mukharamova, N.; Lapkin, D.; Zaluzhnyy, I. A.; Andre, A.; Lazarev, S.; Kim, Y. Y.; Sprung, M.; Kurta, R. P.; Schreiber, F.; Vartanyants, I. A.; Scheele, M., Revealing Grain Boundaries and Defect Formation in Nanocrystal Superlattices by Nanodiffraction. *Small* **2019,** *15* (50), e1904954.

31. Zaluzhnyy, I. A.; Kurta, R. P.; Andre, A.; Gorobtsov, O. Y.; Rose, M.; Skopintsev, P.; Besedin, I.; Zozulya, A. V.; Sprung, M.; Schreiber, F.; Vartanyants, I. A.; Scheele, M., Quantifying Angular Correlations between the Atomic Lattice and the Superlattice of Nanocrystals Assembled with Directional Linking. *Nano Lett* **2017,** *17* (6), 3511-3517.

32. Zaluzhnyy, I. A.; Kurta, R. P.; Scheele, M.; Schreiber, F.; Ostrovskii, B. I.; Vartanyants, I. A., Angular X-Ray Cross-Correlation Analysis (AXCCA): Basic Concepts and Recent Applications to Soft Matter and Nanomaterials. *Materials* **2019,** *12* (21).

33. Kurta, R. P.; Altarelli, M.; Vartanyants, I. A., Structural Analysis by X-Ray Intensity Angular Cross Correlations. In *Advances in Chemical Physics*, 2016; pp 1-39.

34. Carnis, J.; Kirner, F.; Lapkin, D.; Sturm, S.; Kim, Y. Y.; Baburin, I. A.; Khubbutdinov, R.; Ignatenko, A.; Iashina, E.; Mistonov, A.; Steegemans, T.; Wieck, T.; Gemming, T.; Lubk, A.; Lazarev, S.; Sprung, M.; Vartanyants, I. A.; Sturm, E. V., Exploring the 3D structure and defects of a self-assembled gold mesocrystal by coherent X-ray diffraction imaging. *Nanoscale* **2021,** *13* (23), 10425-10435.

35. Kirner, F.; Potapov, P.; Schultz, J.; Geppert, J.; Müller, M.; González-Rubio, G.; Sturm, S.; Lubk, A.; Sturm, E., Additive-controlled synthesis of monodisperse single crystalline gold nanoparticles: interplay of shape and surface plasmon resonance. *Journal of Materials Chemistry C* **2020,** *8* (31), 10844-10851.

36. Sanchez-Iglesias, A.; Grzelczak, M.; Altantzis, T.; Goris, B.; Perez-Juste, J.; Bals, S.; Van Tendeloo, G.; Donaldson, S. H., Jr.; Chmelka, B. F.; Israelachvili, J. N.; Liz-Marzan, L. M., Hydrophobic interactions modulate self-assembly of nanoparticles. *ACS Nano* **2012,** *6* (12), 11059-65.

37. Lapkin, D.; Shabalin, A.; Meijer, J.-M.; Kurta, R.; Sprung, M.; Petukhov, A. V.; Vartanyants, I. A., Angular X-ray cross-correlation analysis applied to the scattering data in 3D reciprocal space from a single crystal. *IUCrJ* **2022,** *9* (4), 425-438.

38. Williamson, G. K.; Hall, W. H., X-ray line broadening from filed aluminium and wolfram. *Acta Metallurgica* **1953,** *1* (1), 22-31.

ToC figure:

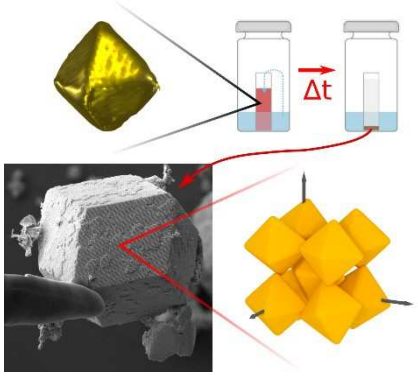

The ToC entry:

A synthesis procedure for PS-SH functionalized gold octahedral nanoparticles of variable size and polymer chain length on the growth of faceted colloidal crystals is explored. To determine the structure of the mesocrystals a SAXS experiment was performed. It was identified by the AXCCA method that nanocrystals self-assemble in a *bcc* superstructure, in which gold octahedral nanoparticles are predominantly oriented tip-to-tip.